

# GaNDLF: A Generally Nuanced Deep Learning Framework for Scalable End-to-End Clinical Workflows in Medical Imaging

Sarthak Pati<sup>1,2,3,4,5,\*</sup>, Siddhesh P. Thakur<sup>1,2,6,\*</sup>, Megh Bhalerao<sup>1,2</sup>, Spyridon Thermos<sup>1,2,7</sup>, Ujjwal Baid<sup>1,2,3,8</sup>, Karol Gotkowski<sup>1,2,9</sup>, Camila Gonzalez<sup>1,2,9</sup>, Orhun Güley<sup>1,2,10</sup>, İbrahim Ethem Hamamci<sup>1,2,11</sup>, Sezgin Eri<sup>1,2,12</sup>, Caleb Grenko<sup>1,2,3,13</sup>, Brandon Edwards<sup>1,2,14</sup>, Micah Sheller<sup>1,2,14</sup>, Jose Agraz<sup>1,2,15</sup>, Bhakti Baheti<sup>1,2,16</sup>, Vishnu Bashyam<sup>1,2,17</sup>, Parth Sharma<sup>1,2,18</sup>, Babak Haghghi<sup>1,2,19</sup>, Aimilia Gastounioti<sup>1,2,20</sup>, Mark Bergman<sup>1,2,21</sup>, Anirban Mukhopadhyay<sup>1,2,22</sup>, Sotirios A. Tsaftaris<sup>1,2,23</sup>, Bjoern Menze<sup>1,2,24</sup>, Despina Kontos<sup>1,2,25</sup>, Christos Davatzikos<sup>1,2,26</sup>, Spyridon Bakas<sup>1,2,3,27,28,29,2\*</sup>

<sup>a</sup>Center for Biomedical Image Computing and Analytics (CBICA), University of Pennsylvania, Philadelphia, PA, USA

<sup>b</sup>Department of Radiology, Perelman School of Medicine, University of Pennsylvania, Philadelphia, PA, USA

<sup>c</sup>Department of Pathology and Laboratory Medicine, Perelman School of Medicine, University of Pennsylvania, Philadelphia, PA, USA

<sup>d</sup>Department of Informatics, Technical University of Munich, Munich, Germany

<sup>e</sup>Institute for Digital Communications, School of Engineering, University of Edinburgh, West Mains Rd, Edinburgh EH9 3FB, UK

<sup>f</sup>Graphisch-Interaktive Systeme, Technical University of Darmstadt, Darmstadt, Germany

<sup>g</sup>International School of Medicine, Istanbul Medipol University, Istanbul, Turkey

<sup>h</sup>Intel Corporation, Santa Clara, CA, USA

<sup>i</sup>Department of Quantitative Biomedicine, University of Zurich, Zurich, Switzerland

## Abstract

Deep Learning (DL) has greatly highlighted the potential impact of optimized machine learning in both the scientific and clinical communities. The advent of open-source DL libraries from major industrial entities, such as TensorFlow (Google), PyTorch (Facebook), and MXNet (Apache), further contributes to DL promises on the democratization of computational analytics. However, increased technical and specialized background is required to develop DL algorithms, and the variability of implementation details hinders their reproducibility. Towards lowering the barrier and making the mechanism of DL development, training, and inference more stable, reproducible, and scalable, without requiring an extensive technical background, this manuscript proposes the **Generally Nuanced Deep Learning Framework** (GaNDLF). With built-in support for  $k$ -fold cross-validation, data augmentation, multiple modalities and output classes, and multi-GPU training, as well as the ability to work with both radiographic and histologic imaging, GaNDLF aims to provide an end-to-end solution for all DL-related tasks, to tackle problems in medical imaging and provide a robust application framework for deployment in clinical workflows.

**Keywords:** Deep Learning, Framework, Segmentation, Regression, Classification, Cross-validation, Data augmentation, Deployment, Clinical, Workflows

## 1. Introduction

Deep Learning (DL) describes a subset of Machine Learning (ML) algorithms built upon the concepts of neural networks [1]. Over the last decade, DL has shown great promise in various problem domains such as semantic segmentation [2–5], quantum physics [6], segmentation of regions of interest (such as tumors) in medical images [7–12], medical landmark detection [13, 14], image registration [15, 16], predictive modelling [17], among many others [18–22]. The majority of this vast research was enabled by the abundance of DL libraries made open source and publicly available, with some of the major ones being TensorFlow (developed by Google) [23] and PyTorch [24] by

\*Equally contributing first authors

\*\*Corresponding author

Email address: [sbakas@upenn.edu](mailto:sbakas@upenn.edu) (Spyridon Bakas<sup>1,2</sup>)

Facebook (originally developed as Caffe [25] by the University of California at Berkeley), which represent the most widely used libraries that facilitated DL research. Among the currently available libraries, PyTorch has proved itself to be one of the most customizable and easily deployable on local workstations through its robust and efficient C++ backend [26].

There have been various efforts by the medical imaging community towards addressing the clinical end-points of academic research, and packaging pre-coded/pre-trained models for data scientists to leverage and address clinical requirements. However, all these efforts, resulting in numerous software packages, can confuse the less experienced user and result in endless hours of searching for the appropriate tool to use. To alleviate this situation, we hereby stratify these efforts into a set of well-defined categories to deepen the community’s understanding. Some of these efforts reside on one side of the spectrum and can be classified as **applications**, since they focus on the end-user, with powerful user interfaces (either graphical, or otherwise). Software packages on the other end of the spectrum can be stratified as **libraries**, since they are built as a mechanism to access low-level machine functionality, while other packages that fall in the middle layer between these two ends, provide a layer of abstraction to enable research and can be classified as **toolkits**. Finally, other software packages can be classified as **frameworks**, since they fulfil various roles and attempt to provide a multitude of functions targeting both developers and end-users. Examples of such packages are the Medical Imaging Interaction Toolkit (MITK) [27] and the Cancer Imaging Phenomics Toolkit (CaPTk) [28–32]. **GaNDLF** also falls into this latter category, with a notably unique emphasis to DL. Figure 1 illustrates this stratification, while also providing some pertinent examples.

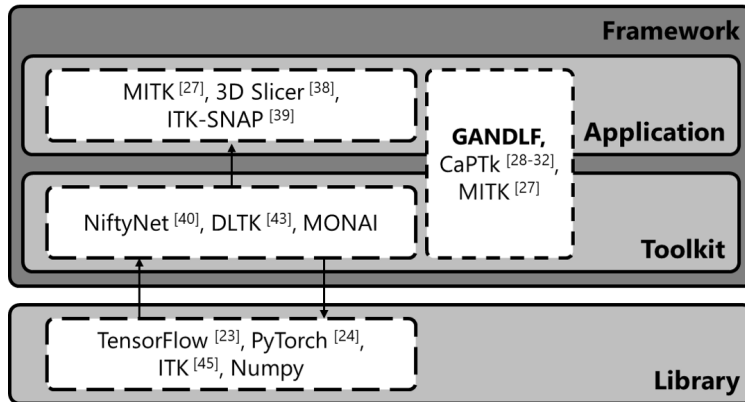


Figure 1: Schematic capturing the categorization of software packages in the open source community.

Ensuring DL algorithms follow similar paradigms would make them more accessible to *clinical researchers* and this would greatly benefit the current scientific paradigm by increasing their clinical impact. Towards this end, developing and making publicly available an open source **user-focused** framework, is expected to allow training and inferring DL algorithms without the need to code, while adhering to best practices established by the greater ML community. Specifically, these practices include (i) nested cross-validation [33–35], and (ii) artificial augmentation of training data [36, 37]. Such a framework, incorporating capabilities to handle **end-to-end** processing (i.e., pre- and post-processing steps) in a cohesive and reproducible manner, would be tremendously useful, and would contribute greatly in democratizing ML (and particularly DL) in the field of medical imaging. Additionally, having a framework that can work across different tasks (segmentation, regression, and classification) and varying diagnostic modalities (radiographic and histologic) would take precision diagnostics to the next frontier of quantitative integrative diagnostics.

Some of these efforts are non-DL based such as MITK [27], 3D Slicer [38], ITK-SNAP [39], and CaPTk [28–32], which have been lauded for their generalizability but fall short when it comes to competitive performance for specific challenges. Towards obtaining superior performance, various efforts concentrating on DL have been devised by the

community, such as NiftyNet [40]<sup>1</sup>, DeepNeuro [41]<sup>2</sup>, ANTsPyNet [42]<sup>3</sup>, and DLTK [43]<sup>4</sup> that are implemented in TensorFlow, as well as pymia<sup>5</sup> [44], InnerEye<sup>6</sup> [45], and MONAI<sup>7</sup> that are implemented in PyTorch. However, all these applications, toolkits, and frameworks (*i*) describe *developer-focused* tools targeting members of the advanced computational research community, (*ii*) can be difficult to grasp by researchers without sufficient experience in DL, (*iii*) do not make it easy for DL scientific developers to write their architectures in a generalizable way, allowing their application on problems spanning across domains, (*iv*) make it difficult to write training pipelines for different problem domains, (*v*) they put the onus of training robust and generalizable models to the user’s knowledge of the training mechanism and the dataset in question, and (*vi*) they lack a single end-to-end application programming interface (API) for training and inference that can span across various problem domains.

In this manuscript, we introduce **GaNDLF** (a **G**enerAlly **ND**eep **L**earning **F**ramework) to enable researchers to solve problems involving segmentation, regression, classification, and synthesis, while producing robust DL models without requiring much knowledge of DL or coding experience. We have developed GaNDLF in PyTorch/Python, as an abstraction layer that incorporates widely used open source libraries (such as Insight Toolkit (ITK)<sup>8</sup> [46] for handling most I/O operations and basic image processing routines, and TorchIO<sup>9</sup> [47] for data augmentation) that can help researchers generate robust DL models quickly and reliably, facilitating reproducibility [48, 49] and being consistent with the criteria of findability, accessibility, interoperability, and reusability (FAIR) [50]. Furthermore, the flexibility of its codebase allows GaNDLF to be used across medical imaging modalities (e.g., 3D radiology scans, and 2D histology whole slide images), with scope for integrating other clinical data (such as genomics and electronic health records) in the future.

## 2. Methods

The intention behind the development of GaNDLF is to provide an end-to-end solution for training robust DL models to tackle a variety of tasks, such as segmentation, regression, and classification, in both 2D and 3D image datasets. It is also designed to work across radiology data (e.g., Magnetic Resonance Imaging (MRI), Computed Tomography (CT), Positron Emission Tomography (PET)) and digitized histology whole slide images (WSI) (e.g., Hematoxylin and Eosin (H&E) stained tissue sections), including specialized image pre-processing functionalities for both. The notable difference between these images is the relatively small resolution and size of radiology images (typically occupying a few megabytes of disk space), compared with the histology WSI that are images of relatively large resolution (150K × 150K pixels), where a single image can occupy 30-40 gigabytes. This enables researchers to use a single package across virtually all medical imaging modalities without performing any additional coding, thereby enabling future studies that rely on integrative diagnostics [51]. Owing to the flexibility of the data loading mechanism in GaNDLF, it could also be possible to integrate genomic data into a model towards further contributing in the field of personalized medicine.

### 2.1. Pre-processing

Providing robust pre-processing techniques, widely applicable to medical imaging data, is critical for such a general-purpose framework to succeed. GaNDLF offers most of the pre-processing techniques reported in the literature, leveraging the capabilities of basic standardized pre-processing routines from ITK [46], and advanced pre-processing functionality from the Cancer Imaging Phenomics Toolkit (CaPTk)<sup>10</sup> [28–32]. The main pre-processing steps for data curation (including harmonization and normalization) are described below.

---

<sup>1</sup><https://github.com/NifTK/NiftyNet>

<sup>2</sup><https://github.com/QTIM-Lab/DeepNeuro>

<sup>3</sup><https://github.com/ANTsX/ANTsPyNet>

<sup>4</sup><https://github.com/DLTK/DLTK>

<sup>5</sup><https://pymia.readthedocs.io/>

<sup>6</sup><https://www.microsoft.com/en-us/research/project/medical-image-analysis/>

<sup>7</sup><https://monai.io/>

<sup>8</sup><https://itk.org/>

<sup>9</sup><https://github.com/fepegar/torchio/>

<sup>10</sup><https://www.cbica.upenn.edu/captk>

1. Data harmonization:

- *Voxel-resolution harmonization*: To ensure that the physical definition of the input data is in a common space (for example, all images can have the voxel resolution of  $I_{res} = [1.0, 1.0, 2.0]$ ).
- *Image-resolution harmonization*: To ensure that the input data has the same image dimensions (for example, all images can be resampled to  $I_{dim} = [240, 240, 155]$ ).

2. Intensity normalization:

- *Thresholding*: To consider pixel/voxel values that belong to a specific intensity range and ignore values below/above this range, by making them equal to zero (Eq.1):

$$x_i = \begin{cases} 0 & x_i < threshold_{min} \\ 0 & x_i > threshold_{max} \\ x_i & otherwise \end{cases} \quad (1)$$

- *Clipping*: To consider pixel/voxel values that belong to a specific intensity range and convert values below/above this range, by making them equal to the minimum/maximum threshold, respectively (Eq.2):

$$x_i = \begin{cases} threshold_{min} & x_i < threshold_{min} \\ threshold_{max} & x_i > threshold_{max} \\ x_i & otherwise \end{cases} \quad (2)$$

- *Rescaling*: To consider all pixel/voxel values after converting them to a common profile (for example, all input images are rescaled to  $[0, 1]$ ).
- *Z-score normalization*: A widely used technique for data normalization in medical imaging [52, 53], that preserves the complete signal of the input image by subtracting the mean and then dividing by the standard deviation of the complete intensity range found in this image. Notably, the application of z-score normalization through GaNDLF can occur either on the full image or only within a masked region of interest, adding to the overall flexibility of this transform.

## 2.2. Data Augmentation

DL methods are well-known for being extremely data hungry [54, 55] and in medical imaging, data is scarce because of various technical, privacy, cultural/ownership concerns, as well as data protection regulatory requirements, such as those set by the Health Insurance Portability and Accountability Act (HIPAA) of the United States [56] and the European General Data Protection Regulation (GDPR) [57]. This necessitates the addition of robust data augmentation techniques [58] into the training data, so that models can gain knowledge from larger datasets and hence be more generalizable to unseen data [59].

GaNDLF leverages an existing robust data augmentation package, namely TorchIO [47]<sup>11</sup>, which provides augmentation transformations in a PyTorch-based mechanism (Table 1). GaNDLF specifically focuses on TorchIO over other packages (such as Batch Generators [60] and Albumentations [61]), because TorchIO provides an easier API for storing extraneous image information. Such information include the affine transform of the image that is critical for maintaining correct physical definition of radiology scans. Furthermore, TorchIO also maintains a strong tie-in with PyTorch’s Tensor data structure, thereby making it relatively easier to extend the data loading with different data formats. More details on the available types of augmentations through GaNDLF are shown in Table 1, and examples of their effects are illustrated in Figure 2, using a brain tumor T2-weighted-Fluid-Attenuated Inversion Recovery (T2-FLAIR) MRI scan from the BraTS challenge’s dataset [9, 11, 62–64].

---

<sup>11</sup><https://torchio.rtfd.io/>

Table 1: All available data augmentations provided in GaNDLF.

Type	Augmentation	Description of Specific Application
Spatial	Affine	Random affine transformations
	Elastic	Dense random elastic deformations
	Flipping	Reversal of the order of elements in an image along the given axes
	Rotation	Rigid rotations of 90 or 180 degrees across the specified axes
	Anisotropic	Down-sample and up-sample images along the provided axes
Intensity	Blur	Blurring using a random-sized Gaussian filter
	Noise	Gaussian noise with random parameters
	Gamma	Random change of contrast by raising values to the power of $\gamma$
MRI Space	Bias field	Random MRI bias field artifact
	MRI motion	Random motion artifact
	Ghosting	Random ghosting artifact
	Spike	Random spike artifacts

### 2.3. Cross-Validation ( $k$ -fold)

$k$ -fold cross validation [65, 66] is a useful technique in ML that ensures reporting unbiased performance estimates and helps capture information from an entire given dataset, by training  $k$  different models on corresponding folds of the complete training data. Specifically, to ensure robust model training, and providing unbiased performance estimates and quantitative validation of the generalization performance of the implemented algorithms (i.e., by evaluating results on new unseen data), GaNDLF offers a nested  $k$ -fold cross validation schema [67], i.e., a well-established way of evaluating algorithms on new datasets [68]. Specifically, during this nested  $k$ -fold cross validation, all data are combined into a single cohort with a model configuration of three sets. Initially cases of the complete cohort are proportionally and randomly divided into  $k$  non-overlapping equally-sized subsets and during each fold,  $k - 1$  of these subsets are considered as the retrospective/discovery cohort and 1 as the prospective/replication cohort, which is unseen for this specific fold. Note that during each fold, the prospective/replication cohort is a different subset. This cross-validation scheme is analyzing the given data as if it had independent discovery and replication cohorts, but in a more statistically robust manner by randomly permuting across all given data. Put differently, in this cross-validation scheme, the implemented algorithms are trained in the discovery set (90% of the data) and then evaluated to the replication set (10% of the data). In other words, the first level of split is to ensure randomization of the testing data (also known as *replication cohort*), and the second level of split is to ensure randomization of validation data (also known as *discovery cohort*). The number of folds for each level of split is specified in the configuration file, and the models for different folds can be trained in parallel (in accordance with the user’s computation environment). GaNDLF also offers the option of specifying single fold training, if so desired.

### 2.4. Training Mechanism

GaNDLF provides a flexible mechanism for training DL models, with support for multiple imaging modalities and output classes, along with support for both 2D and 3D datasets. The main entry point of GaNDLF’s training mechanism is a CSV file provided by the user, through the command line interface. The expected CSV file should comprise the subject identifiers along with the corresponding full paths of all required input images and masks (i.e., for segmentation tasks) and the values required for training and follow up predictions (i.e., for regression and classification tasks). The subject identifiers are used to randomly split the entire dataset into training, validation, and testing subsets, using  $k$ -fold cross-validation [69] (see Section 2.3 for more details). Furthermore, a YAML-based configuration file is used to control and parameterize all aspects of the training, such as the proportional split of the cross-validation, data pre-processing, data augmentations (e.g., type, parameters, and probabilities), model parameters (e.g., architecture, list of classes, final convolution layer, optimizer type, loss function, number of epochs, scheduler, learning rate, batch size), along with the training queue parameters (i.e., samples to extract per volume, maximum queue length, and number of threads to use). The YAML-based configuration file requires an indication of the GaNDLF version used to create the trained model, and the actual trained model, with the intention of ensuring coherence between these two.

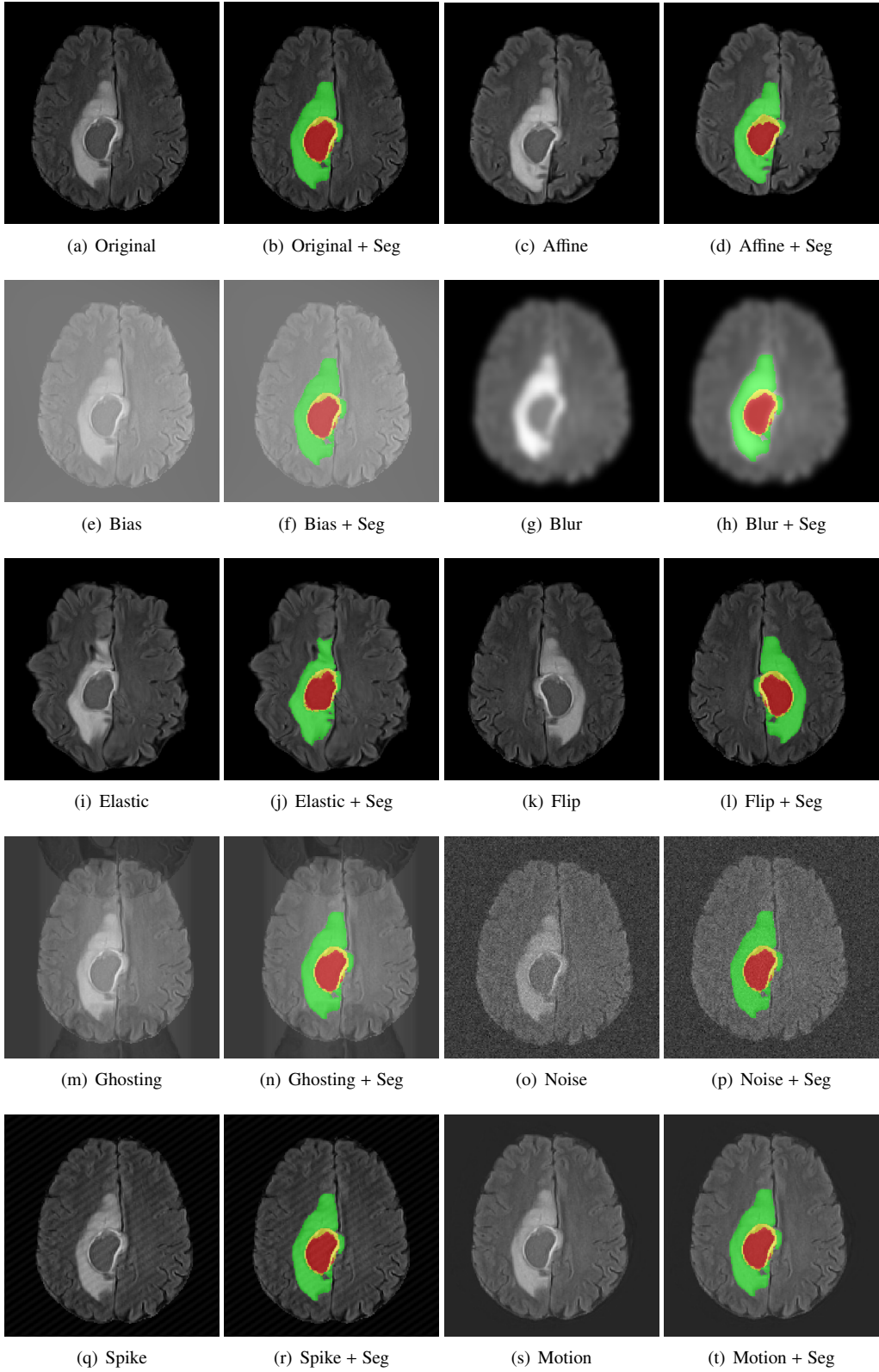


Figure 2: Data augmentation abilities in GaNDLF using TorchIO [47]. Illustrated examples on a brain tumor T2-FLAIR MRI scan, from the BraTS challenge’s dataset.

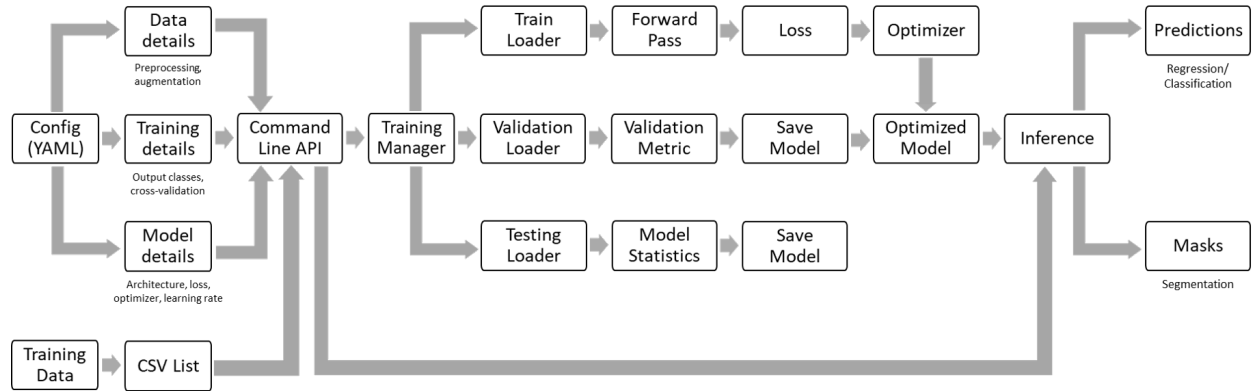


Figure 3: Flowchart depicting the overall training procedure pipeline offered in GaNDLF.

GaNDLF also supports mixed precision training [70] to save computational resources and reduce training time. A single epoch comprises training the model using the training portion of the data and backpropagating the generated loss, followed by evaluating the model performance on the validation portion of the data. In addition to saving the model trained after every epoch, each model corresponding to the best global losses for the training, validation, and testing datasets is also saved. These saved models can be used for subsequent inference, either using a single independent model or in a aggregated fashion utilizing label fusion. Training statistics (such as the *Dice* similarity coefficient and loss) are stored for each epoch, for both the validation and the testing data, in the form of a comma-separated text file (CSV), with the intention of facilitating simplified results reporting and detailed debugging. The overall pipeline of the training procedure offered in GaNDLF is illustrated in Figure 3.

## 2.5. Inference Mechanism

GaNDLF's inference mechanism follows the same paradigm as its training mechanism, where the user needs a CSV file comprising of the subjects' identifiers and the full paths of images, along with a YAML configuration file and the location of the trained models. For each trained model, the corresponding estimated output is stored and (depending on the user's parameterization) a final predicted output is generated by aggregating the outputs of the independent models. This aggregation happens through different approaches, subject to the prediction task, e.g., a label fusion approach may be used for segmentation tasks, averaging for regression tasks, and majority voting for classification. If the full paths of the ground truth labels are given in the input CSV, then the overall metrics (e.g., *Dice* and loss) of the model's performance are also calculated and stored.

### 2.5.1. ...for Radiology scans

As soon as the data is read into memory, GaNDLF applies the pre-processing steps defined in the configuration file to each input dataset (see Section 2.1 for examples of these steps). Then TorchIO’s [47] inference mechanism is used to enable patch-based inference for radiology images. This entails patch extraction, usually of the same size as the one that the corresponding model has been trained on, from the image(s) on which the model needs to infer on. The forward pass of the model is then applied and the result is stored in the corresponding location (Figure 4). This enables models to be trained and inferred on varied patch sizes based on the available hardware resources. Overlapping patches can be stitched by either cropping or taking an average of the predictions at the overlapping area, and the amount of overlap can be specified to ensure that dense inference can occur [47]. Although patch-based training and inference is being widely used, we note that various potential adverse effects of this process have been reported [71].

### 2.5.2. ...for Histology WSIs

Histology WSIs need a different mechanism for inference than that for training, primarily due to their increased hardware requirements, i.e., WSIs can reach 40GB while on-memory. Figure 5(a) illustrates this inference mechanism, which starts with the extraction of a WSI's imaging data at the maximum magnification/resolution (e.g., 40 $\times$ ) and its conversion to a TIFF with 9-10 layers of tiled images with different magnification levels (i.e., Figure 5(a).(ii)-(iii) -

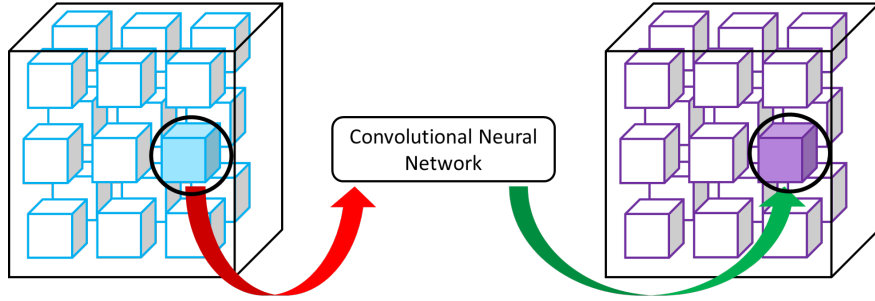


Figure 4: Patch-based inference mechanism in GaNDLF for radiology images.

“Data Fixing Pipeline”). The background area is then filtered out through the generation of a ‘tissue mask’ (Figure 5(a).(iv)), using Red-Blue-Green (RGB) and Otsu-based thresholding [72, 73], which is necessitated by the need to correctly tackle image reading issues occurring when trying to buffer any magnification level other than the lowest (Figure 5(b)). This ‘tissue mask’ also reduces the search space for downstream analyses, and hence reduces the overall computational footprint. This mask is used to calculate foreground coordinates (Figure 5(a).(v)), around which patches are extracted *on-the-fly* by leveraging OpenSlide’s [74] dynamic read region property (Figure 5(a).(vi)). This also produces a ‘count map’ (Figure 5(a)(viii)), which accounts for the contribution of overlapping patches for a tissue region ensuring probabilities are always between 0 and 1. The trained model is then used for a forward pass on each of these patches, producing an independent prediction for each. These predictions are then stitched together to form a ‘segmentation probability map’ (Figure 5(a)(ix)). The ‘segmentation probability map’ and the ‘count map’ are then multiplied to generate the ‘final segmentation’ output (Figure 5(a)(x)).

## 2.6. Modularity and Extendability

This section describes the modularity and extendability of GaNDLF’s functionality. A description of the software stack of GaNDLF is provided, as well as how the lower level libraries are utilized to create an abstract user interface, which can be customized based on the application at hand. Following this, the flexibility of the framework from a technical point-of-view is chronicled, which illustrates the ease with which new functionality can be added.

### 2.6.1. Software Stack

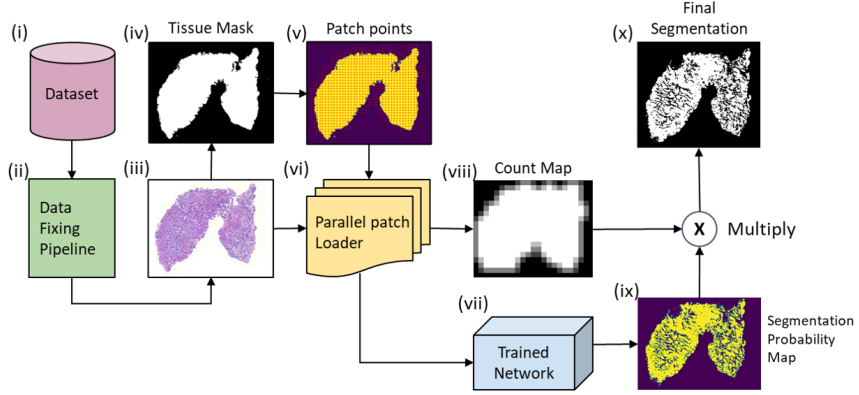
The software stack of GaNDLF is illustrated in Figure 6, depicting the inter-connections between the lower level libraries and more abstract functionalities exposed to the user via the command line interface. This ensures that a researcher can perform DL training and/or inference without having to write a single line of code. Furthermore, the flexibility of the stack is demonstrated by the ease with which a new component (e.g., a pre-processing step, or a new network architecture) can be incorporated into the framework, and subsequently applied to new types of data/applications with minimal effort. Specifically, the framework’s flexibility affects components listed in the following subsections.

### 2.6.2. Dimensions

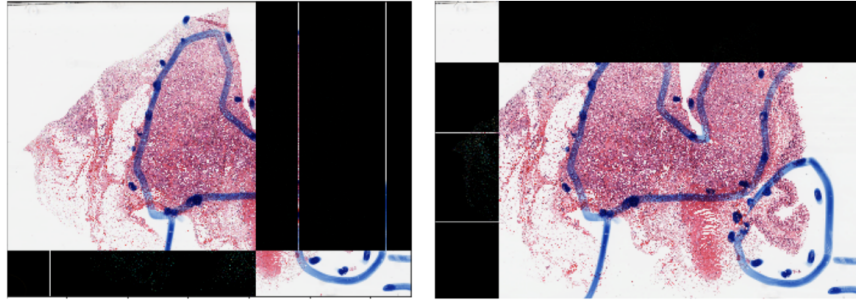
To ensure maximum flexibility and applicability across various types of medical data, GaNDLF supports both 3D and 2D datasets. Using the same codebase, GaNDLF has the ability to apply various architectures across diverse modalities such as MRI, CT, retinal, and digitized histology images, including both immunohistochemical (IHC), Hematoxylin and Eosin (H&E) stained tissue sections.

### 2.6.3. Input channels/modalities & output classes

GaNDLF supports multiple input channels/modalities/sequences and output classes, for either segmentation or regression, to ensure maximal applicability across various problem domains, whether it involves a binary task (e.g., brain extraction) or multi-class tasks (e.g., brain tumor sub-region segmentation).

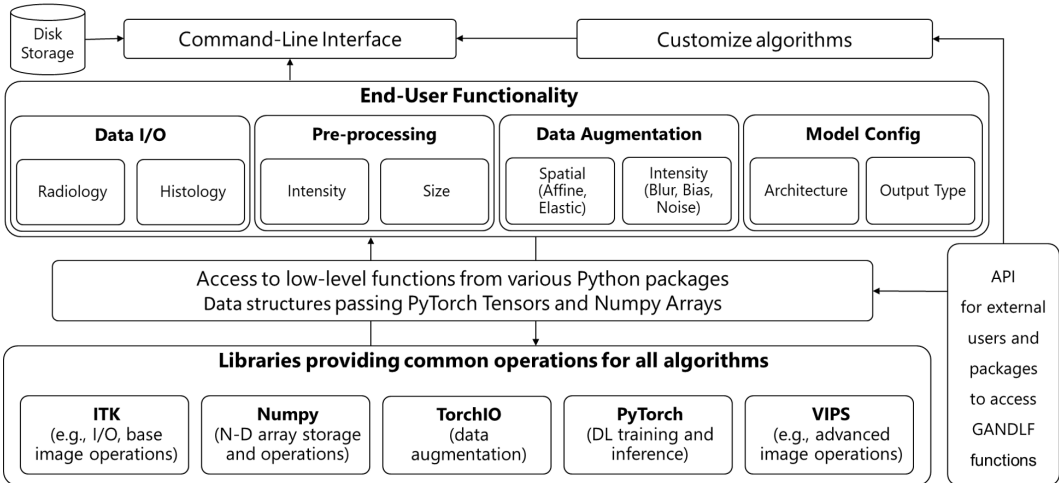


(a) Specialized inference mechanism for WSIs.



(b) Example of a problematic WSI, illustrating data loss in certain patches.

Figure 5: GaNDLF's histology inference mechanism in (a) and illustration of a problematic example in (b), issuing the need for specialized pre-processing. (a) Starting with the raw WSI, multiple specialized pre-processing steps (ii-vi) are performed before a patch can be given as input to a trained model. The coordinates of each patch need to be saved along with the overlap information in order to obtain the final result. (b) Reading data across magnification levels can cause artificial regional data loss.



- *Radiology* images require the ability to process both 2D and 3D data. Although imaging examples that GaNDLF has been applied and evaluated so far describe CT, MRI, and tomosynthesis scans, it offers support for almost every radiologic image via ITK.
- *Histology* images, on the contrary, require specialized handling along the following criteria:
  - **Input:** The use of OpenSlide [74] allows GaNDLF to read a fraction of the entire WSI data at the resolution closest to the requested magnification level, thereby ensuring memory-efficiency.
  - **Patch-extraction:** Since a WSI cannot always be processed on its entirety due to hardware constraints, a patch-based mechanism considering multiple resolutions is essential. This mechanism is offered through our open-source Open Patch Miner (*OPM*)<sup>12</sup>, which has been configured within GaNDLF for simple and rapid batch-processing of patches. OPM can automatically mask tissue in a WSI and convert the highest available resolution to square patches, given a pre-defined overlap amount and patch dimensions. Specifically, it extracts patches with the pre-defined overlap using a pseudo-grid and parallel sampling adjustable for tissue inclusion, in proportion to different tissue classes (for classification tasks), and while omitting the background region.

#### 2.6.4. Network Architectures

- **UNet** without residual connections: The UNet [75] (Figure 7(a), Figure 9) is one of the most well known architectures of Convolutional Neural Networks (CNN) used for 2D and 3D segmentation. The UNet consists of an encoder, comprising convolutional layers and downsampling layers, and a decoder offering upsampling layers (applying transpose convolution layers) and convolutional layers. The encoder-decoder structure contributed in automatically capturing information at multiple scales/resolutions. The UNet further includes skip connections, which consist of concatenated feature maps paired across the encoder and the decoder layer, to improve context and feature re-usability.
- **ResUNet:** This describes a UNet extended with residual connections between the encoder and the decoder to improve the backpropagation process [7, 75–78] (Figure 7(a), Figure 9). Our implementation follows the principle of the UNet architecture, while including skip connections in every convolution block. The residual connections utilize additional information from previous layers (across the encoder and decoder) that enables a boost in the performance.
- **Inception UNet (UInc):** The Inception module [2, 79] can be used to substitute the standard convolutional block (which is a simple series of convolutional layers) of the UNet to create the UInc architecture (Figure 7(d), Figure 12). This module describes parallel pathways of convolutional layers of different kernel sizes, to improve the representation of multi-scale features. UInc has been applied towards semantic segmentation tasks [80].
- **Fully Convolutional Network (FCN):** The FCN architecture [81] (Figure 7(b), Figure 10) introduced in 2017, utilizes hierarchical feature extraction with an encoder recognizing both imaging patterns and spatial information of each input image, with varying receptive fields. FCN has smaller computational requirements compared to UNet, due to the absence of the decoding module, incorporating convolution and transpose convolution operations. FCN simply upsamples the encoded features to the required output segmentations to generate masks. It hence provides faster, yet coarser, segmentations for various domains [82].
- **VGG:** The VGG [83, 84] (Figure 7(c), Figure 11) is a well-known network for performing classification and regression tasks. VGG16 has 16 convolutional layers and 3 dense layers. It is well known for its performance on the ImageNet classification challenge [85]. VGG reinforced the idea that networks should be simple and deep. VGG uses  $3 \times 3$  convolution filters and  $2 \times 2$  max-pooling layers with a stride of 2 throughout the architecture. The original architecture uses ReLU activation function [86] and categorical cross-entropy loss function. The initial layers of the VGG16 perform feature extraction and the last softmax layers act as the classifier. GaNDLF supports multiple variants of the VGG, namely, VGG-11, VGG-13, VGG-16, VGG-19, with and without batch normalization for both 2D and 3D datasets to maximize flexibility.

---

<sup>12</sup><https://github.com/CBICA/OPM>

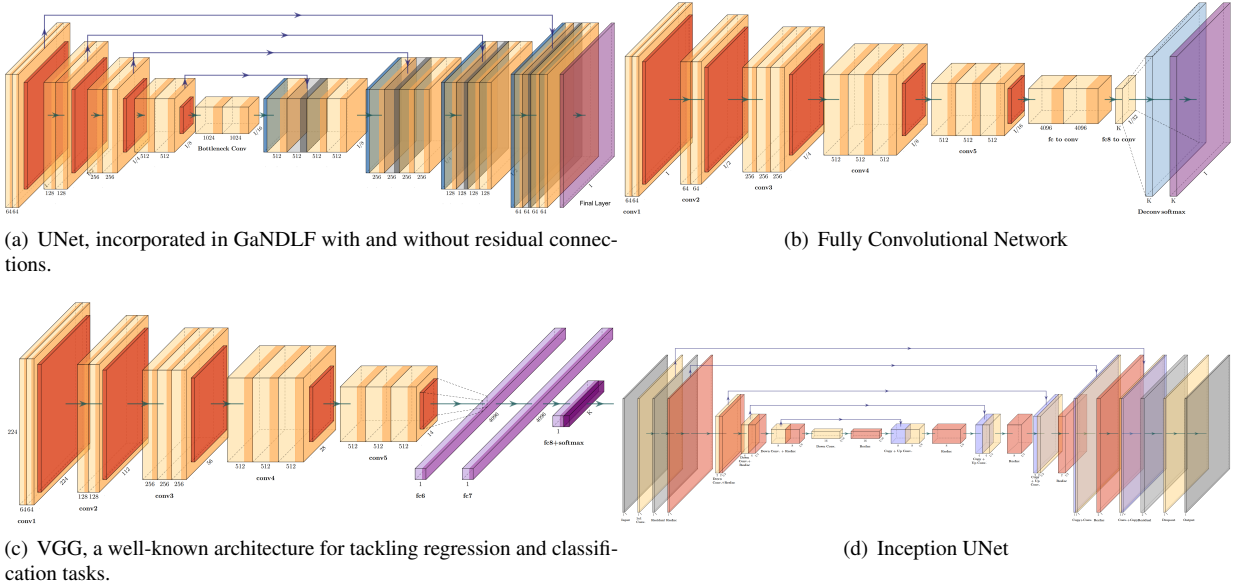


Figure 7: Examples of DL architectures available in GaNDLF for various tasks. Figures were plotted using PlotNeuralNet [87]. Larger figures illustrating each architecture are provided in the Supplementary Material Figures 9-12.

### 2.6.5. Applications

As already mentioned, GaNDLF can train DL models for various tasks, including segmentation, regression, and classification. Depending on available resources, most models can be extended for all these tasks (such as UNet) and there are specialized models that perform specific tasks, such as the brain age prediction model [88], which starts from a VGG-16 model pre-trained on ImageNet weights and is only defined for regression. The flexibility of GaNDLF's framework makes it possible for all these models to co-exist and to leverage the robustly designed data loading and augmentation mechanisms for future extensions of studies. Having a common API for all these tasks also makes it relatively easy for researchers to start applying well-defined network architectures towards various problems and datasets, thereby helping to get DL-based pipelines into clinical workflows.

### 2.7. Interpretability Tools

It is an ongoing problem that deep neural networks lack the interpretability or explainability necessary for medical practitioners to trust into the networks decisions, hindering the practical application of such models in clinical practice [89, 90]. To counter this, GaNDLF integrated the PyTorch library M3D-CAM [91], which enables the easy generation of attention maps of CNN-based models for both 2D and 3D data, and is applicable to both classification and segmentation models. The attention maps can be generated with multiple methods: Guided Back-propagation [92], Grad-CAM [93], Guided Grad-CAM [93] and Grad-CAM++ [94]. The maps visualize the regions in the input data that most heavily influence the model prediction at a certain layer.

### 2.8. Experimental Design and Evaluation

For each application, multiple models are trained in accordance with the cross-validation schema described in Section 2.3. For performance evaluation, we use the model with the best validation score as defined in the application-specific evaluation criteria and apply this model to the test dataset for each fold, giving us the average performance of an architecture for the specific problem. To maintain reproducibility and prevent overfitting, we have trained each architecture with a 20/16/64 split, which results in the training of 25 models in total, for each architecture. Specifically, the 20/16/64 split comprises 5 non-overlapping splits (i.e., each containing 20%) of the complete dataset. Each one of these splits is set aside as the testing cohort for each fold. From the remaining 80% of the complete data during this fold, 5 further splits are done, each containing 16% of the full data, and used for validation. Finally, the remaining data for this fold, which represent 64% of the full cohort, are used for training.

### 2.8.1. Performance Evaluation Metrics

For segmentation tasks, we use the *Dice Similarity Coefficient* [95] (Equation 3) as the performance evaluation metric, and all related models were trained to maximize it. *Dice* is a common metric used to evaluate the performance of segmentation tasks. It measures the extent of spatial overlap, while taking into account the intersection between the predicted masks ( $PM$ ) and the provided ground truth ( $GT$ ), hence handles over- and under-segmentation.

$$Dice = \frac{2|GT \cap PM|}{|GT| + |PM|} \quad (3)$$

For regression and classification tasks, we use the Mean Squared Error ( $MSE$ ) [96] as our evaluation metric and all models were trained to minimize it.  $MSE$  measures the statistical difference between the target prediction  $T$  and the output of the model  $P$  for the entire sample size  $n$ , as illustrated by Equation 4:

$$MSE = \frac{1}{n} \sum_{i=1}^n (T_i - P_i)^2 \quad (4)$$

### 2.8.2. Segmentation of Brain in MRI

Brain extraction is an essential pre-processing step in the realm of neuroimaging, and has an immediate impact on the quality of all subsequent processing and analyses steps. We have used a multi-institutional dataset of  $n = 2520$  MRI scans along with their corresponding manually annotated brain masks. We trained on  $n = 1320$  scans in a modality-agnostic manner (i.e., each structural MRI scan was treated as a separate input) as described in [7] and setting a internal validation set of  $n = 180$  scans, with an independent testing cohort of  $n = 360$  scans to ascertain the model performance. We trained by resampling the data from an isotropic resolution of  $1mm^3$  with a shape of  $240 \times 240 \times 160$  to a anisotropic resolution of  $1.825 \times 1.825 \times 1.25 mm^3$  with a shape of  $128 \times 128 \times 128$  [7]. The reason for this resampling was GPU memory limitations, i.e., 11GB VRAM. We trained multiple architectures (UNet, ResUNet, FCN) with only z-score normalization by discarding the zero-voxels, with no augmentations enabled.

### 2.8.3. Segmentation of Brain Tumor Sub-regions in MRI

Gliomas are among the most common and aggressive brain malignancies and accurate delineation of these regions can provide valuable clinical insights. We have used the publicly available MRI data from the International Brain Tumor Segmentation (BraTS) challenge of 2020 [9, 11, 62–64] to train multiple models to segment the various brain tumor sub-regions. Specifically, we used the full cohort of  $n = 371$  training subjects, which we iteratively split it into  $n = 74$  testing,  $n = 60$  validation, and  $n = 237$  training subjects following the k-fold cross-validation schema mentioned in Section 2.3, with all the 4 structural MRI sequences making up a single input data-point [7]. In total, 25 models are trained for each architecture (UNet, ResUNet, UIInc, and FCN). For each model, we used a set of common hyperparameters that runs in a GPU with 11GB of memory, namely, patch size of  $128 \times 128 \times 128$ , 30 base filters, *Dice* loss, with stochastic gradient descent as the optimizer. For pre-processing, we used z-score normalization by discarding the zero-voxels and cropping of the zero-planes. For data augmentation, we used noise, flipping, affine, rotation and blur, each with a probability of getting picked as 0.35. In each case, the model is trained to maximize the performance evaluation criteria, which is constructed by following the instructions in the Brats challenge [9, 11], i.e., averaging the *Dice* across the enhancing tumor, the tumor core (formed by combining necrosis and enhancing tumor), and the whole tumor (formed by combining the tumor core and the peritumoral edematous/infiltrated tissue).

### 2.8.4. Segmentation of Retinal Fundus

We used the dataset from the PALM challenge [97], which consists of segmentation of lesions in retinal fundus images and replicated the results for a ResUNet architecture from [98]. Additionally, we trained on FCN, UNet, and UIInc to show results from a diversified set of architectures from the same dataset. We used the full cohort of  $n = 400$  training subjects, and iteratively split into  $n = 80$  testing,  $n = 64$  validation, and  $n = 256$  training subjects following the k-fold cross-validation schema mentioned in Section 2.3. In total, 25 models are trained for each architecture (UNet, ResUNet, UIInc, and FCN). For each model, we used a set of common hyperparameters options that runs in a GPU with 11GB of memory, namely, patch size of  $2048 \times 1024$ , 30 base filters, *Dice* loss, with stochastic gradient descent as the optimizer. For pre-processing, we used full-image normalization, and data augmentation was performed using flipping,

rotation, noise and blur, each with a probability of 0.5. The performance is evaluated in comparison with the ground truth binary masks of the fundus in the testing set.

#### 2.8.5. Segmentation of Lung field in CT

An accurate volumetric estimation of the lung field would be crucial towards furthering the clinical goals of tackling respiratory illnesses, such as influenza, pneumonia, and speciality pathologies such as COVID-19. We have used an internal dataset to extract the Lung Field from chest CT images, where we identified  $n = 488$  scans images with their corresponding ground truth. The ground truth annotations were generated under a semi-automatic procedure leveraging 2-cluster k-means, followed by manual qualitative refinements. We then trained on  $n = 244$  scans and internally validated with  $n = 60$  cases. We performed windowed pre-processing and clipped the intensities from  $-900$  to  $-300$  Hounsfield Units (HU). We also resampled the data down to  $128 \times 128 \times 128$  in order to consider the entire chest region and to ensure that the trained model remained agnostic to the original image resolution. We trained the ResUNet architecture with clipping and z-score normalization by discarding the zero-voxels with no augmentations enabled. We use *Dice* as our evaluation metric and trained the model to maximize the *Dice* score.

#### 2.8.6. Segmentation of Quadrants in Panoramic Dental X-Ray Images

Dental enumeration from panoramic dental X-Ray images has a crucial role in the identification of dental diseases. Performing that task with deep learning provides an extensive advantage for the clinician to number the dentition quickly and point out the teeth that need care more accurately. Quadrant segmentation from those panoramic images is the first and the most critical step of numbering the dentition accurately, and a previous study by Yuksel et al. has used an UNet model to achieve that task [99]. Here, we replicated those results by training a segmentation model with GaNDLF that extracts quadrants from the dental X-ray images. To do that, we have used  $n = 900$  dental X-ray images with their corresponding five classes (one for each quadrant plus the background). Class annotations have been generated by the experts and the images were resized down to  $128 \times 128$  in order to consider the entire mouth region. We trained the UNet, the ResUNet, and the FCN architectures with 30 base filters with z-score normalization with no augmentations enabled. We used *Dice* as the evaluation metric and trained the model to maximize it.

#### 2.8.7. Segmentation of Colorectal Cancer in WSI

Colonoscopy pathology examination can find cells of early-stage colon tumor from small tissue slices, and pathologists need to examine hundreds of tissue slices on a day-to-day basis, which is an extremely time consuming and tedious work. The DigestPath challenge [100] motivated participants to automate this process and thereby contribute to potentially improved diagnostics. The data provided in the DigestPath challenge includes slides containing colorectal cancer in JPEG format. The dimensions of the provided images range from  $3000 \times 3000$  to  $30000 \times 30000$ . 180000 patches of the shape  $512 \times 512$  at  $10\times$  resolution were extracted for training and 30000 for validation, with a set of  $n = 30$  WSIs being kept separate as independent testing dataset. We trained the ResUNet architecture, and prior to training we normalized the training values to  $0 - 1$  by dividing each pixel by the maximum possible intensity, i.e., 255. To account for model generalizability, we employed the flip, rotate, blur, noise, gamma, and brightness data augmentations. We used *Dice* as our evaluation metric and trained the model to maximize it. Inference was then done on the testing dataset and the output of the model was evaluated against the ground truth binary masks to calculate the *Dice* score.

#### 2.8.8. Brain Age Prediction from MRI

The human brain ages differently because of various environment factors. Quantifying the difference between actual age and predicted age can provide a useful insight into the overlap of aging signatures with various neurodegenerative pathologies. A 2020 study by Bashyam et al. [88] has used common 2D CNN architectures, borrowed from the computer vision community, to predict brain age from T1-weighted MRI scans across a wide age range. Methodologically, the original fully connected layers of the VGG-Net was replaced by a global average pooling, followed by a new fully connected layer of size 1024 with 80% dropout, and then a single output node with a linear activation was added. The network was then trained with the Adam optimizer, while using MSE. This study was evaluated on 10,000 diverse structural brain MRI scans, pooling data from various studies, including the UK Biobank [101] and a multisite schizophrenia consortium [102], thereby representing various subject populations and acquisition protocols. This

inherent variability of the collective dataset allowed to successfully learn a regression model generalizable across sites. The Bashyam et al. study [88] goes on to examine using the learned age prediction weights as a starting point for transfer learning to other neuroimaging tasks. It is shown that the age prediction weights serve as a superior basis for transfer learning compared to ImageNet, particularly in neuroimaging tasks where the new training data is limited [88].

Leveraging the modular nature of GaNDLF, we replicated the age prediction results of that study [88] using the same model architecture, training schema, and dataset as in the original study, while following GaNDLF’s procedures. Using the VGG-16 model architecture and GaNDLF’s built-in cross-validation functionality, we trained regression models using the intermediate  $n = 80$  axial slices of each subject, with input data being split on the subject level. The same network hyperparameters were used, as those specified in the original study [88].

### 3. Results

Following the procedure described in the experimental design section above, we perform evaluation specific to each application and organ system. For each application, the performance metrics are generated as an average of all the models trained across the cross-validated (see Section 2.3 for details) data splits, which ensures stable model performance without overfitting to a specific data split.

#### 3.0.1. Segmentation of Brain in MRI

In accordance with the experimental protocol highlighted in Section 2.8.2, we have trained 25 models across various data splits for each architecture under consideration. In our analysis, we observed (Table 2) that the ResUNet architecture gave the best results, with the average *Dice* coming to  $0.98 \pm 0.01$ . The UNet and FCN performed favorably as well, each producing an average *Dice* of  $0.97 \pm 0.01$ .

#### 3.0.2. Segmentation of Brain Tumor Sub-regions in MRI

According to the experimental design described in Section 2.8.3, we have trained 25 models across various data splits for each architecture under consideration. We calculated the *Dice* of the predicted multi-label mask with the ground truth annotation for each model by averaging the *Dice* from the 3 clinically relevant regions [11, 62], namely, the enhancing tumor, the tumor core, and the whole tumor. In our analysis, we observed (Table 2) that the ResUNet architecture gave the best results, with the average *Dice* coming to  $0.71 \pm 0.05$ , followed by UNet with  $0.65 \pm 0.05$ , and then UIInc with  $0.64 \pm 0.05$ , with FCN showing the worst performance with *Dice* equal to  $0.62 \pm 0.05$  across all the cross-validation folds.

#### 3.0.3. Segmentation of Retinal Fundus

Following the experimental protocol described in Section 2.8.4, we have trained 25 models across various data splits for each architecture under consideration. In our analysis, we observed (Table 2) that the ResUNet architecture gave the best results, with the average *Dice* coming to  $0.71 \pm 0.05$ , followed by UNet with  $0.65 \pm 0.05$ , and then UIInc with  $0.64 \pm 0.05$ , with FCN being inferior with  $0.62 \pm 0.05$  across all the cross-validation folds.

#### 3.0.4. Segmentation of Lung field in CT

Pursuing the experimental protocol described in Section 2.8.5, we have trained 5 models across a various data splits for the ResUNet architecture under consideration. In our analysis, we observed (Table 2) that the ResUNet gave satisfactory results for the problem with average *Dice* of  $0.95 \pm 0.02$  across all cross-validation folds.

#### 3.0.5. Segmentation of Quadrants in Panoramic Dental X-Ray Images

Following the experimental protocol described in Section 2.8.6, we have trained  $n = 25$  models across various data splits for each architecture under consideration. As shown in Table 2, our analysis showed that the UNet architecture gave the best results, with the average *Dice* coming to  $0.91 \pm 0.01$ . The ResUNet and FCN performed favorably as well, producing an average *Dice* of  $0.88 \pm 0.01$ , and  $0.85 \pm 0.02$ , respectively.

### 3.0.6. Segmentation of Colorectal Cancer in WSI

Following the experimental protocol described in Section 2.8.7, we have trained 1 model across a single data split for the ResUNet architecture. As shown in Table 2, our analysis showed that the ResUNet gave the most satisfactory results for the problem with average *Dice* of  $0.78 \pm 0.03$  for the unseen testing data.

### 3.0.7. Brain Age Prediction from MRI

Following the experimental protocol described in Section 2.8.8, we have trained a custom VGG16 (see Section 2.6 for details) network to predict the age of a brain from a single MR slice, by replicating the results shown in [88]. With an average *MSE* of 0.0141 (Table 3), the prediction quality of the models trained by GaNDLF was in line with the original publication, showcasing the flexibility of GaNDLF to successfully adapt to various problem domains.

Table 2: Results for Semantic Segmentation for some anatomies. The *Organ* describes the organ system of the data, *Application* describes the use case for the trained model(s), *Dimensions* describe the dimensionality for each input modality, *Input Modalities* describes the total number of input modalities for the model to train on, *Output Classes* shows the number of classes the model should be predicting, *Architecture* describes the network topology, and *Loss Metric* describes the type and average value of the selected loss (*Dice* describes the overall testing *Dice* similarity coefficient for the particular model).

Organ	Application	Dimensions	Input Modalities	Output Classes	Architecture	Loss Metric		
						Type	Average Value	
Brain	Brain Extraction	3	1: T1, T1Gd, T2, T2-FLAIR are passed as separate inputs	1	UNet	Dice	$0.97 \pm 0.01$	
					ResUNet	Dice	$0.98 \pm 0.01$	
			FCN		Dice	$0.97 \pm 0.01$		
	Tumor sub-region Segmentation		4: T1, T1Gd, T2, T2-FLAIR	3	UNet	Dice	$0.65 \pm 0.05$	
					ResUNet	Dice	$0.71 \pm 0.05$	
					FCN	Dice	$0.62 \pm 0.05$	
Eye	Fundus Segmentation	2	1: RGB Fundus Images	1	UNet	Dice	$0.85 \pm 0.04$	
					ResUNet	Dice	$0.90 \pm 0.05$	
					FCN	Dice	$0.81 \pm 0.04$	
					UInc	Dice	$0.83 \pm 0.03$	
Lung	Lung Field Segmentation	3	1: CT	1	ResUNet	Dice	$0.95 \pm 0.02$	
Dental	Quadrant Segmentation	2	1: X-Ray	4	UNet	Dice	$0.91 \pm 0.01$	
					ResUNet	Dice	$0.88 \pm 0.01$	
					FCN	Dice	$0.85 \pm 0.02$	
Colon	Colorectal Cancer Segmentation	2	1: Histology H&E	1	ResUNet	Dice	$0.78 \pm 0.03$	

Table 3: Results for Regression of some anatomies. The *Organ* describes the organ system of the data, *Application* describes the use case for the trained model(s), *Dimensions* describe the input dimensionality for each input modality, *Input Modalities* describes the total number of input modalities for the model to train on, *Output Classes* shows the number of classes the model should be predicting, *Architecture* describes the network topology, and *Loss Metric* describes the type and average value of the selected loss (*MSE* corresponds to Mean Squared Error).

Organ	Application	Dimensions	Input Modalities	Output Classes	Architecture	Loss Metric	
						Type	Average Value
Brain	Age Prediction	2	1: Slices of T1 MR	1	Specialized	MSE	$0.0141 \pm 0.01$

### 3.1. Interpretability Tools

The integration of M3D-CAM into GaNDLF allows the generation of these attention maps by simply enabling M3D-CAM in the configuration file. Examples of attention maps generated by M3D-CAM are illustrated in Figure 8.

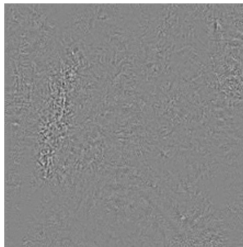
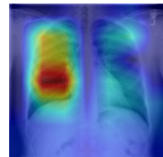
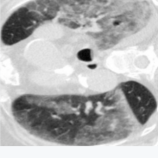
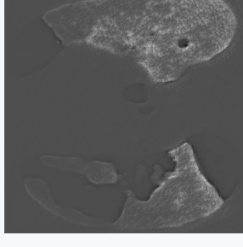
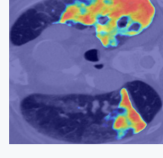
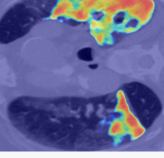
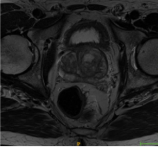
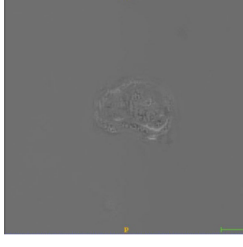
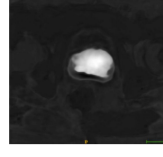
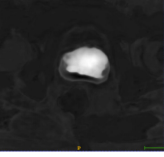
	Image	Guided backpropagation	Grad-Cam	Guided Grad-Cam	Grad-Cam++
#1 Classification (2D)					
#2 Segmentation (2D)					
#3 Segmentation (3D)					

Figure 8: Examples of generated M3D-CAM attention maps [91] with the Grad-CAM backend. The left image shows the attention from a 2D classification network, the middle image from a 2D segmentation network and the right image from a 3D segmentation network.

## 4. Discussion & Conclusions

We have presented the Generally Nuanced Deep Learning Framework (GaNDLF) as an end-to-end solution for scalable clinical workflows in medical imaging. GaNDLF’s contribution spans across its ability to: i) speak directly to the non-DL experts, by providing building blocks for method development; ii) speak to the DL developers allowing for harmonized I/O (i.e., common data loaders enabling the main focus kept on the algorithmic development); iii) process images of various domains, including both radiology scans and digitized histology WSIs; iv) enable work on segmentation, regression, and classification; v) offer built-in general-purpose functionality for augmentations, and cross-validation; vi) be evaluated on a multitude of applications; vii) enable parallel training by using generic high performance computing protocols; viii) integrate tools to promote the interpretability and explainability of DL networks.

The central premise of GaNDLF is to enable researchers to conduct DL research across problem domains (segmentation, regression, classification, synthesis) and modalities (radiology, histology) without worrying about the details such as robust data splitting for training, validation, and testing, and implementing various loss functions. For DL method/architecture developers, GaNDLF provides a mechanism for robust evaluation of their architecture across a wide array of medical datasets that span across various dimensions, channels/modalities, and prediction classes, as well

as to compare their algorithm's performance with well-established built-in architectures, including UNet [75, 78], UNet with residual connections [76], and Inception modules (UInc) [2, 79], as well as a fully convolutional network [81]. For a novice researcher, this framework ensures the easy creation of robust models using various architectures that can be used for scientific research and method discovery, including the potential for aggregating results from various models, which has been shown to provide greater accuracy [9, 11]. For an experienced computational researcher, GaNDLF provides a platform to distribute their methods that allows for their application across various problem domains with relative ease.

Furthermore, we envision the **model zoo** (potentially in collaboration with DAGsHub<sup>13</sup>) in GaNDLF to potentially be a phenomenal resource for pre-trained models and corresponding configurations to replicate training parameters for the scientific community in general. GaNDLF is a fully self-contained DL framework that contains various abstraction layers to enable researchers to produce and contribute robust DL models with **absolutely** zero knowledge of DL or coding experience.

Although GaNDLF has been evaluated across imaging modalities (on radiology and histology images), so far it has been limited to tasks of segmentation and regression, and not for classification or synthesis. Expanding the application areas would bolster the applicability of the framework. Additionally, application to datasets representing analysis of longitudinal images (such as perfusion imaging) has not yet been evaluated. Also, a mechanism to ensure cascading of models (i.e., train/infer different models of same/different architectures sequentially) or aggregation (i.e., train/infer models of different architectures concurrently) is not present, which have generally shown to produce better results [103, 104]. Mechanisms that enable AutoML [105–107] and other network architecture search (NAS) techniques [108] are tremendously powerful tools that create robust models, but are currently not supported in GaNDLF. Finally, application of GaNDLF to other modalities, such as genomics or electronic health records (EHR), has not been explored yet but it is considered as current work in progress.

As a stand-alone package, GaNDLF provides end-to-end functionality that facilitates DL research. Because of its flexible architecture, it is possible to leverage either certain parts of GaNDLF in other packages or leverage other tools and packages such as the community-based Project MONAI<sup>14</sup> to further extend the functionality of GaNDLF. Furthermore, GaNDLF could partner with container-based platforms (such as the BraTS algorithmic repository<sup>15,16</sup>, or ModelHub.AI<sup>17</sup> [20]) towards a structured dissemination of DL models to the research community. As all development is open-sourced<sup>18</sup>, with robust continuous integration and testing courtesy Azure DevOps<sup>19</sup>, contributions from the community will ensure that this framework builds ties to other packages quickly and in a reliable manner for end users.

## Acknowledgements

Research reported in this publication was partly supported by the National Cancer Institute (NCI), the National Institute of Neurological Disorders and Stroke (NINDS), the National Institute on Aging (NIA), the National Institute of Mental Health (NIMH), and the National Institute of Biomedical Imaging and Bioengineering (NIBIB) of the National Institutes of Health (NIH), under award numbers NCI:U01CA242871, NCI:U24CA189523, NINDS:R01NS042645, NIA:RF1AG054409, NIA:U01AG068057, NIMH:R01MH112070, and NIBIB:R01EB022573. The content of this publication is solely the responsibility of the authors and does not represent the official views of the NIH.

<sup>13</sup><https://dagshub.com/>

<sup>14</sup><https://monai.io/>

<sup>15</sup><https://github.com/BraTS>

<sup>16</sup><https://hub.docker.com/u/brats/>

<sup>17</sup><http://modelhub.ai/>

<sup>18</sup><https://github.com/CBICA/GaNDLF/>

<sup>19</sup><https://dev.azure.com/>

## References

### References

- [1] L. K. Hansen, P. Salamon, Neural network ensembles, *IEEE transactions on pattern analysis and machine intelligence* 12 (10) (1990) 993–1001.
- [2] C. Szegedy, W. Liu, Y. Jia, P. Sermanet, S. Reed, D. Anguelov, D. Erhan, V. Vanhoucke, A. Rabinovich, Going deeper with convolutions, in: *Proceedings of the IEEE conference on computer vision and pattern recognition*, 2015, pp. 1–9.
- [3] A. Garcia-Garcia, S. Orts-Escalano, S. Oprea, V. Villena-Martinez, P. Martinez-Gonzalez, J. Garcia-Rodriguez, A survey on deep learning techniques for image and video semantic segmentation, *Applied Soft Computing* 70 (2018) 41–65.
- [4] F. Lateef, Y. Ruichek, Survey on semantic segmentation using deep learning techniques, *Neurocomputing* 338 (2019) 321–348.
- [5] R. Kemker, C. Salvaggio, C. Kanan, Algorithms for semantic segmentation of multispectral remote sensing imagery using deep learning, *ISPRS journal of photogrammetry and remote sensing* 145 (2018) 60–77.
- [6] P. Baldi, P. Sadowski, D. Whiteson, Searching for exotic particles in high-energy physics with deep learning, *Nature communications* 5 (1) (2014) 1–9.
- [7] S. Thakur, J. Doshi, S. Pati, S. Rathore, C. Sako, M. Bilello, S. M. Ha, G. Shukla, A. Flanders, A. Kotrotsou, et al., Brain extraction on mri scans in presence of diffuse glioma: Multi-institutional performance evaluation of deep learning methods and robust modality-agnostic training, *NeuroImage* 220 (2020) 117081.
- [8] J. D. Rudie, D. A. Weiss, R. Saluja, A. M. Rauschecker, J. Wang, L. Sugrue, S. Bakas, J. B. Colby, Multi-disease segmentation of gliomas and white matter hyperintensities in the brats data using a 3d convolutional neural network, *Frontiers in Computational Neuroscience* 13 (2019) 84.
- [9] S. Bakas, M. Reyes, A. Jakab, S. Bauer, M. Rempfler, A. Crimi, R. T. Shinohara, C. Berger, S. M. Ha, M. Rozycski, et al., Identifying the best machine learning algorithms for brain tumor segmentation, progression assessment, and overall survival prediction in the brats challenge, *arXiv preprint arXiv:1811.02629*.
- [10] D. Shen, G. Wu, H.-I. Suk, Deep learning in medical image analysis, *Annual review of biomedical engineering* 19 (2017) 221–248.
- [11] B. H. Menze, A. Jakab, S. Bauer, J. Kalpathy-Cramer, K. Farahani, J. Kirby, Y. Burren, N. Porz, J. Slotboom, R. Wiest, et al., The multimodal brain tumor image segmentation benchmark (brats), *IEEE transactions on medical imaging* 34 (10) (2014) 1993–2024.
- [12] O. H. Maghsoudi, A. Gastounioti, L. Pantalone, C. Davatzikos, S. Bakas, D. Kontos, O-net: An overall convolutional network for segmentation tasks, in: *International Workshop on Machine Learning in Medical Imaging*, Springer, 2020, pp. 199–209.
- [13] F. C. Ghesu, B. Georgescu, T. Mansi, D. Neumann, J. Hornegger, D. Comaniciu, An artificial agent for anatomical landmark detection in medical images, in: *International conference on medical image computing and computer-assisted intervention*, Springer, 2016, pp. 229–237.
- [14] J. Zhang, M. Liu, D. Shen, Detecting anatomical landmarks from limited medical imaging data using two-stage task-oriented deep neural networks, *IEEE Transactions on Image Processing* 26 (10) (2017) 4753–4764.
- [15] J. Borovec, J. Kybic, I. Arganda-Carreras, D. V. Sorokin, G. Bueno, A. V. Khvostikov, S. Bakas, I. Eric, C. Chang, S. Heldmann, et al., Anhir: automatic non-rigid histological image registration challenge, *IEEE Transactions on Medical Imaging*.
- [16] H. Li, Y. Fan, Non-rigid image registration using self-supervised fully convolutional networks without training data, in: *2018 IEEE 15th International Symposium on Biomedical Imaging (ISBI 2018)*, IEEE, 2018, pp. 1075–1078.
- [17] H. Akbari, S. Rathore, S. Bakas, M. P. Nasrallah, G. Shukla, E. Mamourian, M. Rozycski, S. J. Bagley, J. D. Rudie, A. E. Flanders, et al., Histopathology-validated machine learning radiographic biomarker for noninvasive discrimination between true progression and pseudo-progression in glioblastoma, *Cancer* 126 (11) (2020) 2625–2636.
- [18] L. Deng, D. Yu, Deep learning: methods and applications, *Foundations and trends in signal processing* 7 (3–4) (2014) 197–387.
- [19] S. Pouyanfar, S. Sadiq, Y. Yan, H. Tian, Y. Tao, M. P. Reyes, M.-L. Shyu, S.-C. Chen, S. Iyengar, A survey on deep learning: Algorithms, techniques, and applications, *ACM Computing Surveys (CSUR)* 51 (5) (2018) 1–36.
- [20] A. Hosny, M. Schwier, C. Berger, E. P. Örnek, M. Turan, P. V. Tran, L. Weninger, F. Isensee, K. H. Maier-Hein, R. McKinley, et al., Modelhub.ai: Dissemination platform for deep learning models, *arXiv preprint arXiv:1911.13218*.
- [21] M. J. Sheller, G. A. Reina, B. Edwards, J. Martin, S. Bakas, Multi-institutional deep learning modeling without sharing patient data: A feasibility study on brain tumor segmentation, in: *International MICCAI Brainlesion Workshop*, Springer, 2018, pp. 92–104.
- [22] M. J. Sheller, B. Edwards, G. A. Reina, J. Martin, S. Pati, A. Kotrotsou, M. Milchenko, W. Xu, D. Marcus, R. R. Colen, et al., Federated learning in medicine: facilitating multi-institutional collaborations without sharing patient data, *Scientific reports* 10 (1) (2020) 1–12.
- [23] M. Abadi, P. Barham, J. Chen, Z. Chen, A. Davis, J. Dean, M. Devin, S. Ghemawat, G. Irving, M. Isard, et al., Tensorflow: A system for large-scale machine learning, in: *12th {USENIX} symposium on operating systems design and implementation ({OSDI} 16)*, 2016, pp. 265–283.
- [24] A. Paszke, S. Gross, F. Massa, A. Lerer, J. Bradbury, G. Chanan, T. Killeen, Z. Lin, N. Gimelshein, L. Antiga, et al., Pytorch: An imperative style, high-performance deep learning library, in: *Advances in neural information processing systems*, 2019, pp. 8026–8037.
- [25] Y. Jia, E. Shelhamer, J. Donahue, S. Karayev, J. Long, R. Girshick, S. Guadarrama, T. Darrell, Caffe: Convolutional architecture for fast feature embedding, *arXiv preprint arXiv:1408.5093*.
- [26] A. Milioto, C. Stachniss, Bonnet: An open-source training and deployment framework for semantic segmentation in robotics using cnns, in: *2019 International Conference on Robotics and Automation (ICRA)*, IEEE, 2019, pp. 7094–7100.
- [27] I. Wolf, M. Vetter, I. Wegner, M. Nolden, T. Bottger, M. Hastenteufel, M. Schobinger, T. Kunert, H.-P. Meinzer, The medical imaging interaction toolkit (mitk): a toolkit facilitating the creation of interactive software by extending vtk and itk, in: *Medical Imaging 2004: Visualization, Image-Guided Procedures, and Display*, Vol. 5367, International Society for Optics and Photonics, 2004, pp. 16–27.
- [28] C. Davatzikos, S. Rathore, S. Bakas, S. Pati, M. Bergman, R. Kalarot, P. Sridharan, A. Gastounioti, N. Jahani, E. Cohen, et al., Cancer imaging phenomics toolkit: quantitative imaging analytics for precision diagnostics and predictive modeling of clinical outcome, *Journal of medical imaging* 5 (1) (2018) 011018.

[29] S. Pati, A. Singh, S. Rathore, A. Gastounioti, M. Bergman, P. Ngo, S. M. Ha, D. Bounias, J. Minock, G. Murphy, et al., The cancer imaging phenomics toolkit (captk): Technical overview, in: International MICCAI Brainlesion Workshop, Springer, 2019, pp. 380–394.

[30] S. Rathore, S. Bakas, S. Pati, H. Akbari, R. Kalarot, P. Sridharan, M. Rozycski, M. Bergman, B. Tunc, R. Verma, et al., Brain cancer imaging phenomics toolkit (brain-captk): an interactive platform for quantitative analysis of glioblastoma, in: International MICCAI Brainlesion Workshop, Springer, 2017, pp. 133–145.

[31] S. Rathore, S. Mohan, S. Bakas, C. Sako, C. Badve, S. Pati, A. Singh, D. Bounias, P. Ngo, H. Akbari, et al., Multi-institutional noninvasive in vivo characterization of idh, 1p/19q, and egfrviii in glioma using neuro-cancer imaging phenomics toolkit (neuro-captk), Neuro-oncology advances 2 (Supplement\_4) (2020) iv22–iv34.

[32] A. Fathi Kazerooni, H. Akbari, G. Shukla, C. Badve, J. D. Rudie, C. Sako, S. Rathore, S. Bakas, S. Pati, A. Singh, et al., Cancer imaging phenomics via captk: multi-institutional prediction of progression-free survival and pattern of recurrence in glioblastoma, JCO clinical cancer informatics 4 (2020) 234–244.

[33] R. Kohavi, et al., A study of cross-validation and bootstrap for accuracy estimation and model selection, in: Ijcai, Vol. 14, Montreal, Canada, 1995, pp. 1137–1145.

[34] B. Efron, R. Tibshirani, Improvements on cross-validation: the 632+ bootstrap method, Journal of the American Statistical Association 92 (438) (1997) 548–560.

[35] M. W. Browne, Cross-validation methods, Journal of mathematical psychology 44 (1) (2000) 108–132.

[36] A. Mikolajczyk, M. Grochowski, Data augmentation for improving deep learning in image classification problem, in: 2018 international interdisciplinary PhD workshop (IIPhDW), IEEE, 2018, pp. 117–122.

[37] E. D. Cubuk, B. Zoph, D. Mane, V. Vasudevan, Q. V. Le, Autoaugment: Learning augmentation strategies from data, in: Proceedings of the IEEE conference on computer vision and pattern recognition, 2019, pp. 113–123.

[38] R. Kikinis, S. D. Pieper, K. G. Vosburgh, 3d slicer: a platform for subject-specific image analysis, visualization, and clinical support, in: Intraoperative imaging and image-guided therapy, Springer, 2014, pp. 277–289.

[39] P. A. Yushkevich, Y. Gao, G. Gerig, Itk-snap: An interactive tool for semi-automatic segmentation of multi-modality biomedical images, in: 2016 38th Annual International Conference of the IEEE Engineering in Medicine and Biology Society (EMBC), IEEE, 2016, pp. 3342–3345.

[40] E. Gibson, W. Li, C. Sudre, L. Fidon, D. I. Shakir, G. Wang, Z. Eaton-Rosen, R. Gray, T. Doel, Y. Hu, et al., Niftynet: a deep-learning platform for medical imaging, Computer methods and programs in biomedicine 158 (2018) 113–122.

[41] A. Beers, J. Brown, K. Chang, K. Hoebel, J. Patel, K. I. Ly, S. M. Tolaney, P. Brastianos, B. Rosen, E. R. Gerstner, et al., Deepneuro: an open-source deep learning toolbox for neuroimaging, Neuroinformatics (2020) 1–14.

[42] N. J. Tustison, P. A. Cook, A. J. Holbrook, H. J. Johnson, J. Muschelli, G. A. Devanyi, J. T. Duda, S. R. Das, N. C. Cullen, D. L. Gillen, et al., Antsx: A dynamic ecosystem for quantitative biological and medical imaging, medRxiv.

[43] N. Pawlowski, S. I. Ktena, M. C. Lee, B. Kainz, D. Rueckert, B. Glocker, M. Rajchl, Dltk: State of the art reference implementations for deep learning on medical images, arXiv preprint arXiv:1711.06853.

[44] A. Jungo, O. Scheidegger, M. Reyes, F. Balsiger, pymia: A python package for data handling and evaluation in deep learning-based medical image analysis, Computer methods and programs in biomedicine 198 (2021) 105796.

[45] O. Oktay, J. Nanavati, A. Schwaighofer, D. Carter, M. Bristow, R. Tanno, R. Jena, G. Barnett, D. Noble, Y. Rimmer, et al., Evaluation of deep learning to augment image-guided radiotherapy for head and neck and prostate cancers, JAMA network open 3 (11) (2020) e2027426–e2027426.

[46] M. M. McCormick, X. Liu, L. Ibanez, J. Jomier, C. Marion, Itk: enabling reproducible research and open science, Frontiers in neuroinformatics 8 (2014) 13.

[47] F. Pérez-García, R. Sparks, S. Ourselin, [Torchio: a python library for efficient loading, preprocessing, augmentation and patch-based sampling of medical images in deep learning](https://www.sciencedirect.com/science/article/pii/S0169260721003102), Computer Methods and Programs in Biomedicine (2021) 106236 doi:<https://doi.org/10.1016/j.cmpb.2021.106236>.  
URL <https://www.sciencedirect.com/science/article/pii/S0169260721003102>

[48] V. Stodden, J. Borwein, D. H. Bailey, Setting the default to reproducible, computational science research. SIAM News 46 (5) (2013) 4–6.

[49] R. D. Peng, Reproducible research in computational science, Science 334 (6060) (2011) 1226–1227.

[50] M. D. Wilkinson, M. Dumontier, I. J. Aalbersberg, G. Appleton, M. Axton, A. Baak, N. Blomberg, J.-W. Boiten, L. B. da Silva Santos, P. E. Bourne, et al., The fair guiding principles for scientific data management and stewardship, Scientific data 3 (1) (2016) 1–9.

[51] J. Sorace, D. R. Aberle, D. Elimam, S. Lawvere, O. Tawfik, W. D. Wallace, Integrating pathology and radiology disciplines: an emerging opportunity?, BMC medicine 10 (1) (2012) 1–6.

[52] B. M. Ellingson, T. Zaw, T. F. Cloughesy, K. M. Naeini, S. Lalezari, S. Mong, A. Lai, P. L. Nghiempuu, W. B. Pope, Comparison between intensity normalization techniques for dynamic susceptibility contrast (dsc)-mri estimates of cerebral blood volume (cbv) in human gliomas, Journal of Magnetic Resonance Imaging 35 (6) (2012) 1472–1477.

[53] J. C. Reinhold, B. E. Dewey, A. Carass, J. L. Prince, Evaluating the impact of intensity normalization on mr image synthesis, in: Medical Imaging 2019: Image Processing, Vol. 10949, International Society for Optics and Photonics, 2019, p. 109493H.

[54] G. Chartrand, P. M. Cheng, E. Vorontsov, M. Drozdzal, S. Turcotte, C. J. Pal, S. Kadoury, A. Tang, Deep learning: a primer for radiologists, Radiographics 37 (7) (2017) 2113–2131.

[55] G. Marcus, Deep learning: A critical appraisal, arXiv preprint arXiv:1801.00631.

[56] G. J. Annas, et al., Hipaa regulations-a new era of medical-record privacy?, New England Journal of Medicine 348 (15) (2003) 1486–1490.

[57] P. Voigt, A. Von dem Bussche, The eu general data protection regulation (gdpr), A Practical Guide, 1st Ed., Cham: Springer International Publishing.

[58] C. Shorten, T. M. Khoshgoftaar, A survey on image data augmentation for deep learning, Journal of Big Data 6 (1) (2019) 60.

[59] L. Perez, J. Wang, The effectiveness of data augmentation in image classification using deep learning, arXiv preprint arXiv:1712.04621.

[60] F. Isensee, P. Jäger, J. Wasserthal, D. Zimmerer, J. Petersen, S. Kohl, J. Schock, A. Klein, T. Roß, S. Wirkert, P. Neher, S. Dinkelacker, G. Köhler, K. Maier-Hein, [batchgenerators - a python framework for data augmentation](https://doi.org/10.5281/zenodo.3632567) (Jan. 2020). doi:[10.5281/zenodo.3632567](https://doi.org/10.5281/zenodo.3632567).  
URL <https://doi.org/10.5281/zenodo.3632567>

[61] A. Buslaev, V. I. Iglovikov, E. Khvedchenya, A. Parinov, M. Druzhinin, A. A. Kalinin, Albumentations: fast and flexible image augmentations, *Information* 11 (2) (2020) 125.

[62] S. Bakas, H. Akbari, A. Sotiras, M. Bilello, M. Rozycki, J. S. Kirby, J. B. Freymann, K. Farahani, C. Davatzikos, Advancing the cancer genome atlas glioma mri collections with expert segmentation labels and radiomic features, *Scientific data* 4 (1) (2017) 1–13.

[63] S. Bakas, H. Akbari, A. Sotiras, M. Bilello, M. Rozycki, J. Kirby, J. Freymann, K. Farahani, C. Davatzikos, Segmentation labels and radiomic features for the pre-operative scans of the tcga-gbm collection, *The cancer imaging archive* 286.

[64] S. Bakas, H. Akbari, A. Sotiras, M. Bilello, M. Rozycki, J. Kirby, J. Freymann, K. Farahani, C. Davatzikos, Segmentation labels and radiomic features for the pre-operative scans of the tcga-lgg collection (2017).

[65] D. M. Allen, The relationship between variable selection and data agumentation and a method for prediction, *technometrics* 16 (1) (1974) 125–127.

[66] A. M. Molinaro, R. Simon, R. M. Pfeiffer, *Prediction error estimation: a comparison of resampling methods*, *Bioinformatics* 21 (15) (2005) 3301–3307. [arXiv:<https://academic.oup.com/bioinformatics/article-pdf/21/15/3301/6236941/bti499.pdf>](https://academic.oup.com/bioinformatics/article-pdf/21/15/3301/6236941/bti499.pdf), doi:10.1093/bioinformatics/bti499. URL <https://doi.org/10.1093/bioinformatics/bti499>

[67] G. C. Cawley, N. L. Talbot, On over-fitting in model selection and subsequent selection bias in performance evaluation, *The Journal of Machine Learning Research* 11 (2010) 2079–2107.

[68] R. Duda, Hart, p., e., and stork, dg., “pattern classification”, Nueva York: John Wiley and Sons.

[69] J. Friedman, T. Hastie, R. Tibshirani, *The elements of statistical learning*, Vol. 1, Springer series in statistics New York, 2001.

[70] P. Micikevicius, S. Narang, J. Alben, G. Diamos, E. Elsen, D. Garcia, B. Ginsburg, M. Houston, O. Kuchaiev, G. Venkatesh, et al., Mixed precision training, *arXiv preprint arXiv:1710.03740*.

[71] G. A. Reina, R. Panchumarthy, S. P. Thakur, A. Bastidas, S. Bakas, Systematic evaluation of image tiling adverse effects on deep learning semantic segmentation, *Frontiers in neuroscience* 14 (2020) 65.

[72] M. Niethammer, D. Borland, J. Marron, J. Woosley, N. E. Thomas, Appearance normalization of histology slides, in: *International Workshop on Machine Learning in Medical Imaging*, Springer, 2010, pp. 58–66.

[73] A. Vahadane, A. Sethi, Towards generalized nuclear segmentation in histological images, in: *13th IEEE International Conference on BioInformatics and BioEngineering*, IEEE, 2013, pp. 1–4.

[74] A. Goode, B. Gilbert, J. Harkes, D. Jukic, M. Satyanarayanan, Openslide: A vendor-neutral software foundation for digital pathology, *Journal of pathology informatics* 4.

[75] O. Ronneberger, P. Fischer, T. Brox, U-net: Convolutional networks for biomedical image segmentation, in: *International Conference on Medical image computing and computer-assisted intervention*, Springer, 2015, pp. 234–241.

[76] M. Drozdzal, E. Vorontsov, G. Chartrand, S. Kadoury, C. Pal, The importance of skip connections in biomedical image segmentation, in: *Deep Learning and Data Labeling for Medical Applications*, Springer, 2016, pp. 179–187.

[77] K. He, X. Zhang, S. Ren, J. Sun, Deep residual learning for image recognition, in: *Proceedings of the IEEE conference on computer vision and pattern recognition*, 2016, pp. 770–778.

[78] Ö. Çiçek, A. Abdulkadir, S. S. Lienkamp, T. Brox, O. Ronneberger, 3d u-net: learning dense volumetric segmentation from sparse annotation, in: *International conference on medical image computing and computer-assisted intervention*, Springer, 2016, pp. 424–432.

[79] C. Szegedy, S. Ioffe, V. Vanhoucke, A. Alemi, Inception-v4, inception-resnet and the impact of residual connections on learning, in: *Proceedings of the AAAI Conference on Artificial Intelligence*, Vol. 31, 2017.

[80] J. Doshi, G. Erus, M. Habes, C. Davatzikos, Deepmrseg: a convolutional deep neural network for anatomy and abnormality segmentation on mr images, *arXiv preprint arXiv:1907.02110*.

[81] J. Long, E. Shelhamer, T. Darrell, Fully convolutional networks for semantic segmentation, in: *Proceedings of the IEEE conference on computer vision and pattern recognition*, 2015, pp. 3431–3440.

[82] G. Litjens, T. Kooi, B. E. Bejnordi, A. A. A. Setio, F. Ciompi, M. Ghafoorian, J. A. Van Der Laak, B. Van Ginneken, C. I. Sánchez, A survey on deep learning in medical image analysis, *Medical image analysis* 42 (2017) 60–88.

[83] K. Simonyan, A. Zisserman, Very deep convolutional networks for large-scale image recognition, *arXiv preprint arXiv:1409.1556*.

[84] A. Ben-Cohen, I. Diamant, E. Klang, M. Amitai, H. Greenspan, Fully convolutional network for liver segmentation and lesions detection, in: *Deep learning and data labeling for medical applications*, Springer, 2016, pp. 77–85.

[85] J. Deng, W. Dong, R. Socher, L.-J. Li, K. Li, L. Fei-Fei, Imagenet: A large-scale hierarchical image database, in: *2009 IEEE conference on computer vision and pattern recognition*, Ieee, 2009, pp. 248–255.

[86] A. F. Agarap, Deep learning using rectified linear units (relu), *arXiv preprint arXiv:1803.08375*.

[87] H. Iqbal, *HarisIqbal88/plotneuralnet v1.0.0* (Dec. 2018). doi:10.5281/zenodo.2526396. URL <https://doi.org/10.5281/zenodo.2526396>

[88] V. M. Bashyam, G. Erus, J. Doshi, M. Habes, I. Nasralah, M. Truelove-Hill, D. Srinivasan, L. Mamourian, R. Pomponio, Y. Fan, et al., Mri signatures of brain age and disease over the lifespan based on a deep brain network and 14 468 individuals worldwide, *Brain* 143 (7) (2020) 2312–2324.

[89] A. Holzinger, From machine learning to explainable ai, in: *2018 world symposium on digital intelligence for systems and machines (DISA)*, IEEE, 2018, pp. 55–66.

[90] A. Gastounioti, D. Kontos, Is it time to get rid of black boxes and cultivate trust in ai?, *Radiology: Artificial Intelligence* 2 (3) (2020) e200088.

[91] K. Gotkowski, C. Gonzalez, A. Bucher, A. Mukhopadhyay, M3d-cam: A pytorch library to generate 3d data attention maps for medical deep learning (2020). [arXiv:\[arXiv:2007.00453\]\(https://arxiv.org/abs/2007.00453\)](https://arxiv.org/abs/2007.00453).

[92] J. T. Springenberg, A. Dosovitskiy, T. Brox, M. Riedmiller, Striving for simplicity: The all convolutional net, *arXiv preprint arXiv:1412.6806*.

[93] R. R. Selvaraju, M. Cogswell, A. Das, R. Vedantam, D. Parikh, D. Batra, Grad-cam: Visual explanations from deep networks via gradient-based localization, in: *Proceedings of the IEEE international conference on computer vision*, 2017, pp. 618–626.

[94] A. Chattopadhyay, A. Sarkar, P. Howlader, V. N. Balasubramanian, Grad-cam++: Generalized gradient-based visual explanations for deep convolutional networks, in: *2018 IEEE Winter Conference on Applications of Computer Vision (WACV)*, IEEE, 2018, pp. 839–847.

[95] A. P. Zijdenbos, B. M. Dawant, R. A. Margolin, A. C. Palmer, Morphometric analysis of white matter lesions in mr images: method and validation, *IEEE transactions on medical imaging* 13 (4) (1994) 716–724.

[96] J. O. Berger, *Statistical decision theory and Bayesian analysis*, Springer Science & Business Media, 2013.

[97] H. Fu, F. Li, J. I. Orlando, H. Bogunovic, X. Sun, J. Liao, Y. XU, S. ZHANG, X. ZHANG, Palm: Pathologic myopia challenge, in: *Proc. IEEE Dataport*, 2019, p. 1.

[98] U. Baid, B. Baheti, P. Dutande, S. Talbar, Detection of pathological myopia and optic disc segmentation with deep convolutional neural networks, in: *TENCON 2019-2019 IEEE Region 10 Conference (TENCON)*, IEEE, 2019, pp. 1345–1350.

[99] A. E. Yüksel, S. Gültekin, E. Simsar, S. D. Özdemir, M. Gündoğar, S. B. Tokgöz, İ. E. Hamamci, Dental enumeration and multiple treatment detection on panoramic x-rays using deep learning, *Scientific reports* 11 (1) (2021) 1–10.

[100] J. Li, S. Yang, X. Huang, Q. Da, X. Yang, Z. Hu, Q. Duan, C. Wang, H. Li, Signet ring cell detection with a semi-supervised learning framework, in: *International Conference on Information Processing in Medical Imaging*, Springer, 2019, pp. 842–854.

[101] C. Sudlow, J. Gallacher, N. Allen, V. Beral, P. Burton, J. Danesh, P. Downey, P. Elliott, J. Green, M. Landray, et al., Uk biobank: an open access resource for identifying the causes of a wide range of complex diseases of middle and old age, *Plos med* 12 (3) (2015) e1001779.

[102] M. Rozycki, T. D. Satterthwaite, N. Koutsouleris, G. Erus, J. Doshi, D. H. Wolf, Y. Fan, R. E. Gur, R. C. Gur, E. M. Meisenzahl, et al., Multisite machine learning analysis provides a robust structural imaging signature of schizophrenia detectable across diverse patient populations and within individuals, *Schizophrenia bulletin* 44 (5) (2018) 1035–1044.

[103] O. Araque, I. Corcuera-Platas, J. F. Sánchez-Rada, C. A. Iglesias, Enhancing deep learning sentiment analysis with ensemble techniques in social applications, *Expert Systems with Applications* 77 (2017) 236–246.

[104] X. Dong, Z. Yu, W. Cao, Y. Shi, Q. Ma, A survey on ensemble learning, *Frontiers of Computer Science* 14 (2) (2020) 241–258.

[105] C. Thornton, F. Hutter, H. H. Hoos, K. Leyton-Brown, Auto-weka: Combined selection and hyperparameter optimization of classification algorithms, in: *Proceedings of the 19th ACM SIGKDD international conference on Knowledge discovery and data mining*, 2013, pp. 847–855.

[106] L. Zimmer, M. Lindauer, F. Hutter, Auto-pytorch tabular: Multi-fidelity metalearning for efficient and robust autodl, *IEEE Transactions on Pattern Analysis and Machine Intelligence* (2021) 1–12IEEE early access; also available under <https://arxiv.org/abs/2006.13799>.

[107] H. Mendoza, A. Klein, M. Feurer, J. T. Springenberg, M. Urban, M. Burkart, M. Dippel, M. Lindauer, F. Hutter, Towards automatically-tuned deep neural networks, in: F. Hutter, L. Kotthoff, J. Vanschoren (Eds.), *AutoML: Methods, Systems, Challenges*, Springer, 2018, Ch. 7, pp. 141–156.

[108] T. Elsken, J. H. Metzen, F. Hutter, et al., Neural architecture search: A survey., *J. Mach. Learn. Res.* 20 (55) (2019) 1–21.

## **5. Supplementary Material**

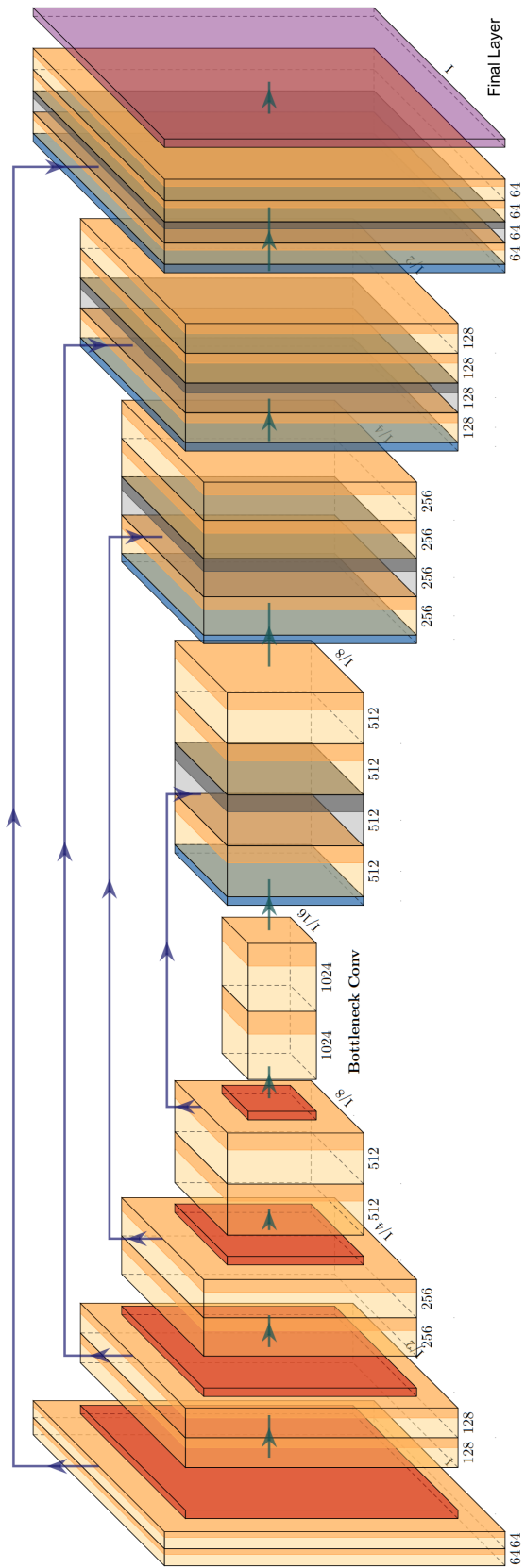


Figure 9: UNet, incorporated in GaNDLF with and without residual connections.

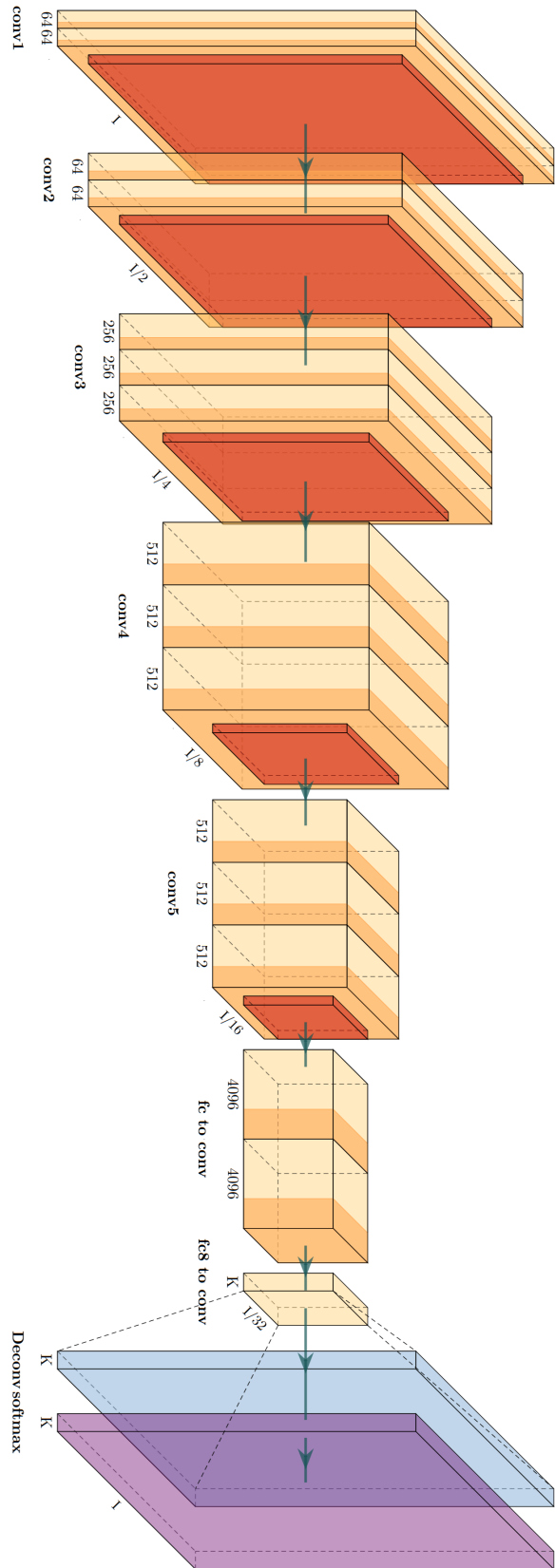


Figure 10: Fully Convolutional Network.

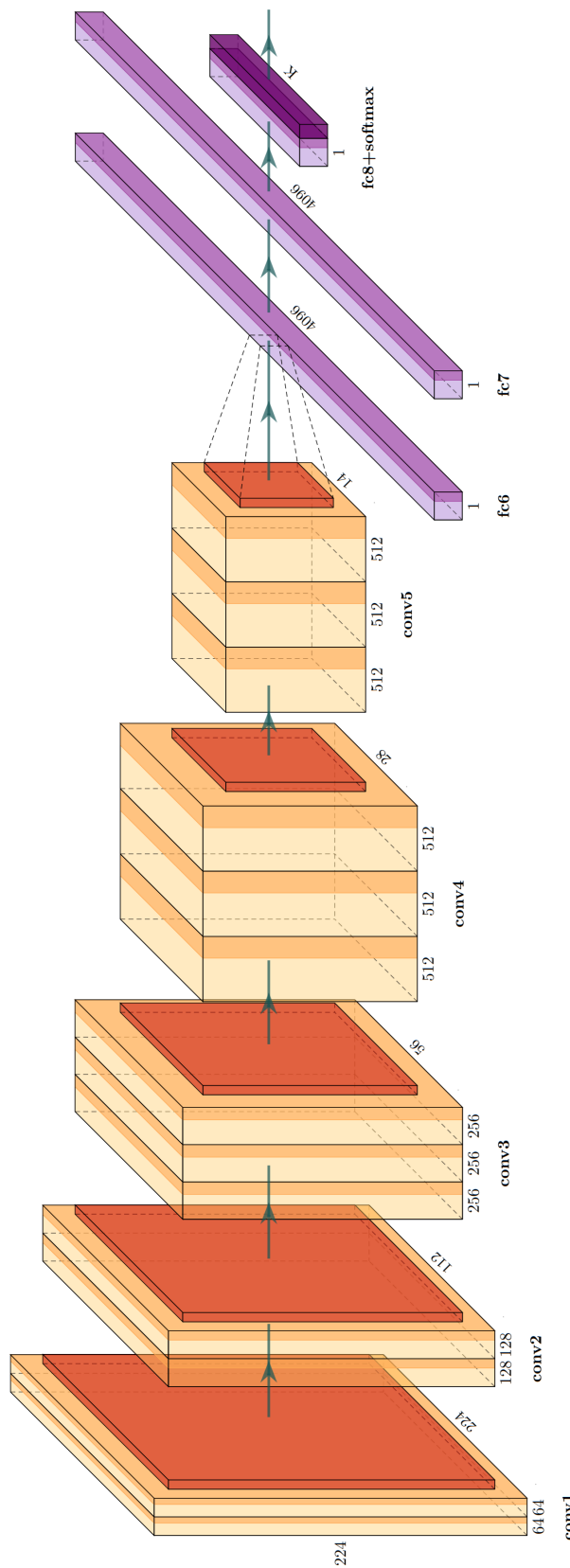


Figure 11: VGG16, a well-known architecture for tackling regression and classification tasks.

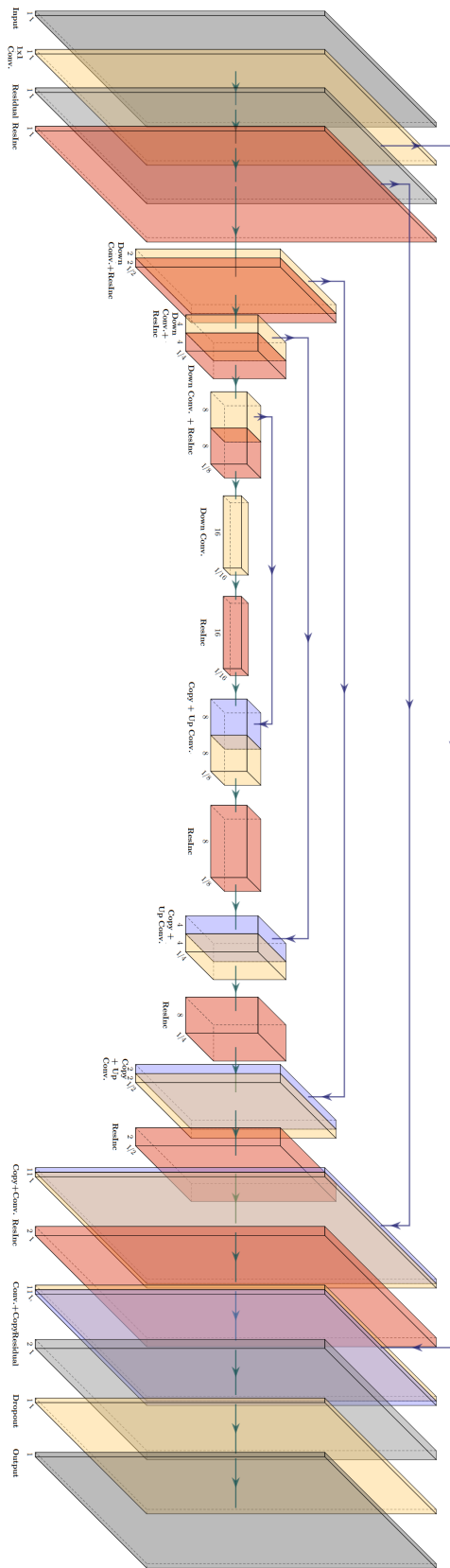


Figure 12: Inception UNet.